



Structural and electrical properties of gadolinium-substituted $\text{La}_{0.6-x}\text{Gd}_x\text{Sr}_{0.4}\text{MnO}_3$ ($x = 0-0.3$)

A. Miri, M. H. Ehsani^a , S. Esmaceli

Faculty of Physics, Semnan University, PO Box: 35195-363, Semnan, Iran

Received: 27 July 2022 / Accepted: 7 December 2022

© The Author(s), under exclusive licence to Società Italiana di Fisica and Springer-Verlag GmbH Germany, part of Springer Nature 2022

Abstract In recent decades, manganites have received much attention due to their various compositions and applications in various fields. This study investigated manganite's structural and electrical properties with the chemical formula $\text{La}_{0.6-x}\text{Gd}_x\text{Sr}_{0.4}\text{MnO}_3$ ($x = 0, 0.25, 0.05, 0.1, \text{ and } 0.3$). All samples were synthesized using the nitrate-complex auto-ignition technique. Structural analysis showed that the crystal structure of these samples is rhombohedral with an R-3c space group at room temperature. The XRD and FESEM image analysis investigated the samples' crystallite and grain size. Measurement of the specific electrical resistance of the samples in the temperature range of 10–350 K and the magnetic fields of 0–9 T showed that the increase in temperature of the electrical resistance first increases and then decreases. All samples' insulation-metal transition temperature (T_{M-I}) moves to lower temperatures with an increasing Gd^{3+} substitution and moves to higher temperatures as the magnetic field increases. In addition to increasing substitution, the electrical resistance also increases due to changes in spin irregularity at the grain boundary and, consequently, the difficulty of the double exchange mechanism. The electrical resistance decreases with increasing magnetic field, followed by the magnetic order created in the samples and the changes in the spin angle between the charge carriers. Finally, the bolometric application and magnetoresistivity of the samples are examined.

1 Introduction

Early studies in manganite perovskite date back to the 1950s, but after discovering the Colossal Magnetoresistance (CMR) effect in 1994, these compounds received much attention [1–4]. In addition to rich physics, these compounds show various unique properties that offer them many applications. Manganites are magnetic materials with a strong electron correlation with the same degree of interaction between their degrees of freedom, i.e., charge, spin, lattice, and circuit based on manganese oxide. These degrees of freedom have caused a great deal of variation in the formation of structural, electrical, and magnetic phases [5, 6]. As a result, manganite nanostructures often have different physical properties than their single-crystal and bulk samples [7, 8]. Nanomanganites with a temperature above room temperature, like $\text{La}_{1-x}\text{Sr}_x\text{MnO}_3$, with an adjustable transition temperature around room temperature, are suitable for medical applications such as cancer treatment and magnetic sensors. Other phenomena, such as the exchange bias effect, are seen in these nanostructures, effective in spintronic components [9, 10]. Critical thermodynamic phenomena are also observed in manganite nanoparticles. As the particle size decreases, the magnetic phase transitions change or disappear [11, 12].

Temperature shift and flattening are other common phenomena in manganite nanostructures. Changing the phase shift reduces thermal and magnetic residues, which are essential for their magnetic coolant [11]. Due to the breaking of atomic bonds on the surface, manganite nanostructures' electrical and magnetic properties become very different from their inner part, the core. In addition, surface effects, internal stresses, and chemical heterogeneities disrupt the competition between supercharging and double exchange interactions and change manganites' electrical and magnetic properties [13–15]. Generally, the surface layer is considered magnetically dead in ferromagnetic nanostructures and reduces electrical conductivity [16]. There are two types of magnetoresistance in manganites. One is known as the CMR effect, which has the highest value in the insulation-metal phase transition temperature and is seen in the magnetic fields of several Tesla orders, which is practically suitable in strong magnetic fields. Another is the intergranular magnetometer resistance seen in polycrystalline samples, which has large values by reducing the grain size to the nanometer scale. This magnetoresistance type is important because it occurs in relatively small magnetic fields [17, 18]. The origin of this type of magnetism is resistance to the sample's magnetic properties, such as the spin scattering of charge carriers at the grain boundary and the wall of magnetic fields and the reduction of tunneling between grains due to the spin polarization of the spin polarization charge carriers. This type of magnetoresistance is seen below the phase transition temperature and in relatively

^a e-mail: Ehsani@semnan.ac.ir (corresponding author)

small magnetic fields, with essential applications in magnetic sensors, spintronic components, spin valves, and magnetic memories [19–21].

Previous studies showed that LaSrMnO₃ (LSMO) nanomanganites have many applications. For example, manganite containing La-doped with 20% Sr is one of the known cathodes that are used as cathodes in solid oxide fuel cells. Another application of nano-manganites is in the field of magnetic refrigerators, which can improve some parameters related to them by reducing the size of the particles. Magnetic sensors and heads use the effect of giant magnetoresistance in mixed capacitance magnetites. Heat therapy to destroy cancer cells, use as drug carriers, and increase contrast in MRI imaging are among the applications of this category of materials in the medical field [22–25]. By substituting different rare earth elements with smaller ionic radii at La-site, the Curie temperature of the LSMO should be reduced to close to ambient temperature without affecting its physical features. When different rare earth elements are substituted at the Sr-site in manganites, the average ionic radius of the Sr-site is altered, changing the transition temperature. In actuality, the substitution (Nd, Eu, Pr, Sm, Gd, etc.) causes the lattice under consideration to experience internal chemical pressure [26, 27]. The Mn–O–Mn bond angles decrease due to the MnO₆ octahedra being deformed due to the chemical pressure created [28]. In addition to increasing the S–L coupling, the increase in bond length reduces lattice disorder [29]. Gadolinium is ferromagnetic. There is no anisotropy in gadolinium because we have symmetrical s. So in this study, the effects of Gd substitution on the structural and electrical properties of La_{0.6–x}Gd_xSr_{0.4}MnO₃ ($x = 0, 0.025, 0.05, 0.1, \text{ and } 0.3$) manganite have been investigated. The XRD and FESEM image analysis were used to investigate the structural properties. The sample's electrical properties are investigated by measuring the samples' resistivity and calculating the bolometric and magnetoresistance properties in terms of temperature. The electrical properties of the samples are investigated in the temperature range of 10–350 K and the magnetic fields of 0 to 9 T. Generally, applying an external magnetic field has a constructive role in the transport of load carriers and reduces the specific strength of the material [30, 31]. Therefore, the maximum magnetic field of up to 9 T was applied in this study.

2 Experimental

A nitrate-complex auto-ignition technique synthesized ceramic La_{0.6–x}Gd_xSr_{0.4}MnO₃. In this synthesis, La(NO₃)₃·6H₂O (Lanthanum(III) nitrate hexahydrate with 99.99% purity), Sr(NO₃)₂ (Strontium nitrate with 99.99% purity), Gd(NO₃)₂ (Gadolinium(III) nitrate with 99.99% purity), and Mn(NO₃)₂·4H₂O (Manganese(II) nitrate with 99.99% purity) were used as pre-materials. The materials are dissolved in deionized water with calculated stoichiometry, respectively. Ethylene glycol (as a polymerizer) and Citric acid were added to the solution. The pH of the solution (constantly stirred) is also kept unchanged at 7 by adding ammonia. The solution was stirred on a hot surface at 100 °C for 8 h to produce a homogeneous solution with a yellowish color. The temperature is then raised to 150 °C for 1 h to allow the gel to burn in a self-combustion process to produce an oxidized product. The product is calcined for 6 h in an electric oven at 500 °C. The samples are placed in a cold press with a diameter of 10 mm and a thickness of 2–3 mm, experiencing a pressure of 20 TON/Cm² to prepare the compounds' tablets. The tablets were sintered at 700 °C for 6 h to study the Gd³⁺ Substitution's effect on the electrical properties of LSMO. The samples at the different substitutions of $x = 0, 0.025, 0.05, 0.1, \text{ and } 0.3$ are named S1, S2, S3, S4, and S5, respectively. In the following, we can see the review and analysis related to the structural and electrical properties of the samples. Structural analysis was performed on prepared powders by X-ray diffraction (XRD) spectrum with Cu-K α irradiation in the range of 10 to 80° in steps of 0.4° at room temperature by the Advanced8 X-ray machine. Particle size was measured using a Field Emission Scanning Electron Microscope (FESEM) by FE-SEM Zeiss (Sigma 300 HV). Finally, the electrical characteristics of the samples are measured by the PPMS device model 6000.

3 Results

3.1 XRD analyses

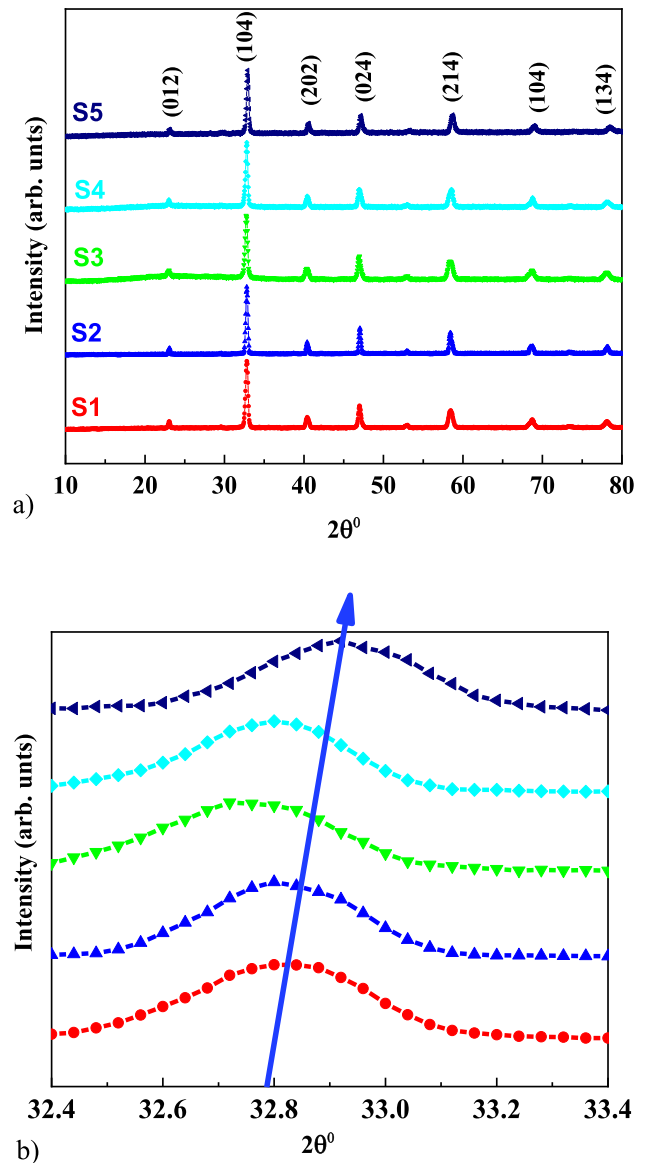
The XRD pattern of La_{0.6–x}Gd_xSr_{0.4}MnO₃ ($x = 0–0.3$) samples is shown in Fig. 1. As shown in Fig. 1, the structures were synthesized without any impurities with the R-3c space group. The Substitution of Gd³⁺ ions in La³⁺ sites can be inferred from the displacement of the diffraction peaks. According to Bragg's Law, the diffraction spectra are shifted to larger angles due to the Substitution of Gd³⁺ in La³⁺ sites. The reason for this shift can be related to the ionic radius of Gd³⁺ (0.938 Å) [32] substitution in La³⁺ (1.032 Å) [32] sites. For better understanding, the displacement of the main peak ($2\theta = 32.8^\circ$) is magnified in Fig. 1b.

Bragg's Law [33] converts observed 2θ positions to d_{hkl} (crystallographic plane distance).

$$2d \sin \theta = m\lambda \quad (1)$$

here, d , θ , m , and λ represent the distance between the planes of the samples, the main characteristic peak, a positive integer ($m = 1$), and the incident wave's wavelength ($\lambda_{Cu} = 1.5406 \text{ \AA}$). The results show that by increasing the amount of Gd³⁺ Substitution from $x = 0$ to $x = 0.3$, the diffraction peaks move to larger angles, which indicate a decrease in the distance between the crystal

Fig. 1 a XRD results of samples and **b** Magnified angle between 32° and 34°



plates from 3.0235 to 3.0131 Å. The results are reported in Table 1. The crystallite size of the samples is calculated by the Scherer equation [34]:

$$D = \frac{K\lambda}{\beta \cos \theta} \tag{2}$$

here, K , β , and θ represent the Scherer’s constant (~ 0.9), the full width at half maximum intensity (FWHM), and the Bragg angle. Table 1 reports the obtained results. Halder–Wagner (H–W) technique has been used to calculate the lattice strain structures [35]. The H–W method is defined using the following equation:

$$\left(\frac{\beta_{hkl}^*}{d_{hkl}^*}\right)^2 = \left(\frac{\varepsilon}{2}\right)^2 + \left(\frac{\beta_{hkl}^*}{d_{hkl}^*}\right)\left(\frac{1}{D}\right) \tag{3}$$

The lattice strain values of the samples are, $\beta_{hkl}^* = \frac{\beta_{hkl} \cos \theta}{\lambda}$, $d_{hkl}^* = \frac{2 \sin \theta}{\lambda}$, and ε . The Halder-Wagner plot of samples is shown in Fig. 2 ($\left(\frac{\beta_{hkl}^*}{d_{hkl}^*}\right)^2$ vs. $\left(\frac{\beta_{hkl}^*}{d_{hkl}^*}\right)$ plot).

Rietveld analysis can be used to study the XRD spectrum further. Rietveld analysis is one of the best ways to fit and link experimental and computational data. In the following, we have examined the samples using Rietveld analysis by MAUD software (Fig. 3). This software converts data obtained from the X-ray diffraction of samples into computational data. Much information such as spatial group, lattice constants, R_{wp} (%), R_b (%), and R_{exp} (%) of samples are obtained using the output of this software, which

Table 1 Structure parameter of $\text{La}_{0.6-x}\text{Gd}_x\text{Sr}_{0.4}\text{MnO}_3$ ($x = 0-0.3$)

Samples	S1	S2	S3	S4	S5
d (Å)	3.0233	3.02315	3.0292	3.0254	3.0131
D_{Scher} (nm)	26.025	30.01	25.15	28.22	27.08
ϵ^* (10^{-2}) ϵ	1.37	0.88	1.89	1.35	1.25
$a = b$ (Å)	5.486	5.487	5.484	5.469	5.450
c (Å)	13.358	13.367	13.353	13.382	13.328
R_{wp} (%)	6.725	7.508	6.856	6.684	5.556
R_{b} (%)	5.224	10.708	12.155	10.022	4.356
R_{exp} (%)	4.988	6.219	4.838	5.404	4.333
GOF = ($R_{\text{wp}}/R_{\text{exp}}$)	1.349	1.207	1.417	1.236	1.282
t	0.986	0.985	0.983	0.978	0.961

is given in Table 1. This method's analysis indicates that the samples have an orthorhombic crystalline structure with an R-3c space group. In Fig. 3, the experimental data are represented by (Y_{obs}), the output information from the XRD device, and the computational data represented by (Y_{calc}) obtained from the software. The green lines are related to the Bragg positions drawn below these two diagrams, and the blue diagram shows the difference between the experimental and computational diffraction schemes ($Y_{\text{obs}} - Y_{\text{calc}}$).

The tolerance factor of the samples was calculated to investigate their crystalline structure. In 1926, Goldschmidt defined the tolerance factor (t) for the ABO_3 perovskite structures as follows [36]:

$$t = \frac{r_A + r_O}{\sqrt{2}(r_B + r_O)} \quad (4)$$

where r_A and r_B are the cation radii of A and B atoms, and r_O is the anionic radii of the O atom. If the tolerance factor is less than one, the $A-O$ and $B-O$ bonds are under tension and pressure, respectively. This distortion in the lattice causes an octahedral rotation θ of oxygen. By increasing the Gd^{3+} atom substitution in the La atom sites, the $\text{La}_{0.6-x}\text{Gd}_x\text{Sr}_{0.4}\text{MnO}_3$ ($x = 0-0.3$) tolerance factor is reduced. Increases in the octahedral rotation angle of oxygen consequently lead to increases in the Mn-O-Mn bond angles. Changes in the Mn-O length and angle of the Mn-O-Mn bond can be related to the lattice distortion of contaminated specimens due to Gd^{3+} Substitution. Changing these two fundamental parameters can significantly affect the electrical properties of the compounds, which will be mentioned in the electrical section.

The obtained results show slight changes in lattice parameters. This slight change in lattice parameters indicates that the lattice modifies to accommodate the occupied Gd^{3+} cations in the La^{3+} site without breaking bonds.

3.2 FESEM analyses

FESEM images were used to study particle morphology and average diameter size detection. The FESEM images in Fig. 4 are for the $\text{La}_{0.6-x}\text{Gd}_x\text{Sr}_{0.4}\text{MnO}_3$ ($x = 0-0.3$) compound in 200 nm scale. As shown in Fig. 4, the particles have deformed from a quasi-spherical state to a polygon. The average diameter size was calculated using Digimizer software. The data obtained using this software was also fitted using the Log-Normal function (Eq. 5).

$$f(D) = \left(\frac{1}{\sqrt{2\pi}\sigma D} \right) \exp \left[-\frac{\ln^2\left(\frac{D}{D_0}\right)}{2\sigma^2} \right] \quad (5)$$

The internal diagram in Fig. 4 shows the data scattering curve. The average diameter and the standard deviation of samples can be calculated by Eqs. 6 and 7, respectively.

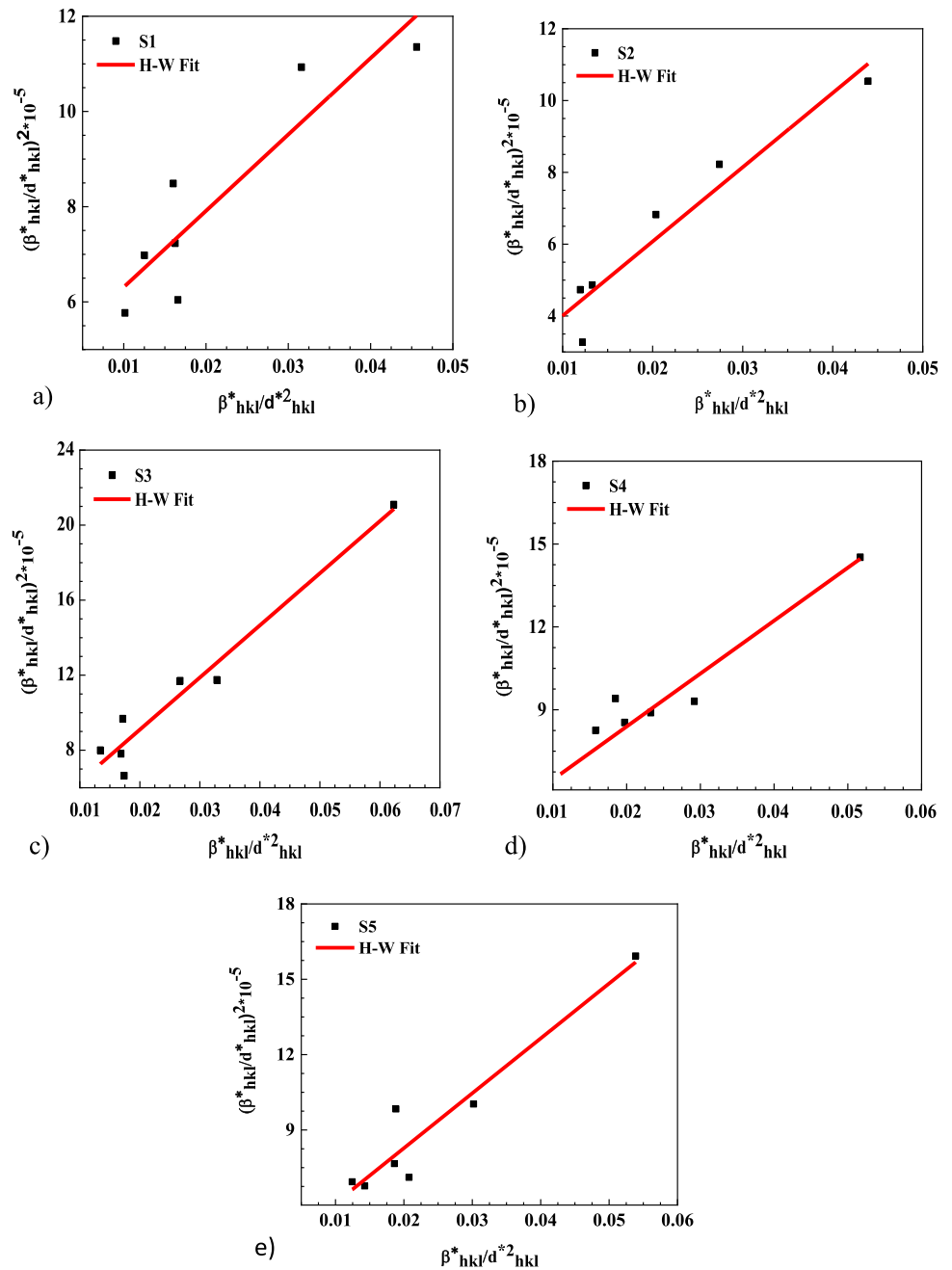
$$\langle D \rangle = D_0 \exp\left(\frac{\sigma^2}{2}\right) \quad (6)$$

$$\sigma_D = \langle D \rangle [\exp(\sigma^2) - 1]^{1/2} \quad (7)$$

where D_0 is the mean diameter and σ is the data scatter, respectively. The results are reported in Table 2. FESEM image analysis illustrates that the average particle size of samples increased by increasing Gd^{3+} ion substitution in LSMO.

The results from FESEM analysis show that the created grains are continuous (glued together). This feature leads to the improvement of their electrical properties.

Fig. 2 Halder–Wagner plot of **a** S1, **b** S2, **c** S3, **d** S4, and **e** S5 samples



3.3 Electrical properties of samples

In this section, the electrical characteristics of $\text{La}_{0.6-x}\text{Gd}_x\text{Sr}_{0.4}\text{MnO}_3$ ($x = 0-0.3$) samples in the temperature range of 10–350 K and 5 magnetic fields (0, 1, 3, 5, 7, and 9 T) is investigated. Considering the dimensions of the sample and its electrical resistance, the specific resistance of the sample can be obtained according to the formula:

$$\rho = \frac{\pi}{\text{Ln}2} \times R \times t \tag{6}$$

where R is the resistance measured by the PPMS device inside the SQUID device, and t is the sample thickness.

Generally, three types of heat energy, anisotropy, and exchange in manganites, compete, and this competition leads to the creation of electrical and magnetic properties and the emergence of transition temperatures. Thermal energy obtained from ambient temperature and anisotropic energy refer to energies required to rotate magnetic moments in matter relative to the direction of its easy axis. Exchange energy, the intrinsic and internal interaction of magnetic ions, is of quantum origin and is obtained from the overlap of particle wave functions.

Fig. 3 Maud refinement of **a** S1, **b** S2, **c** S3, **d** S4, and **e** S5 samples

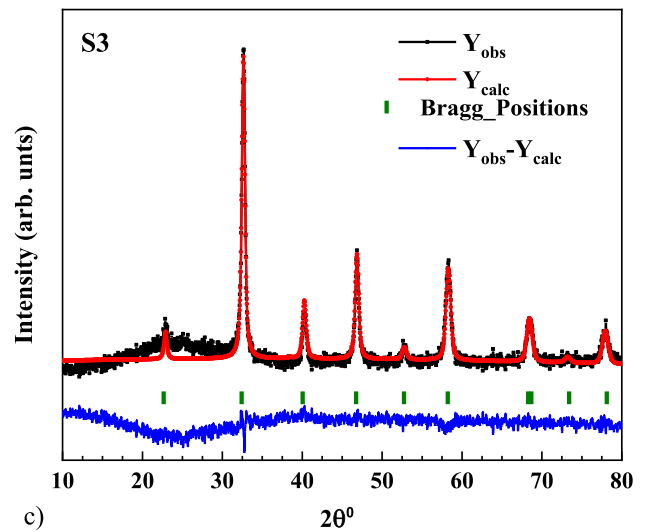
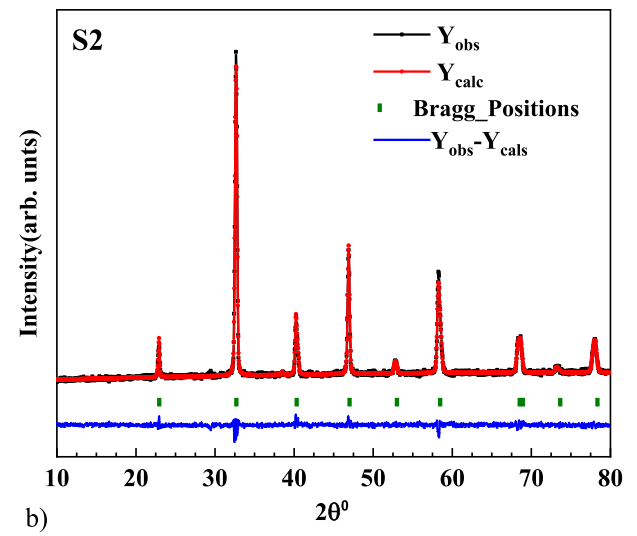
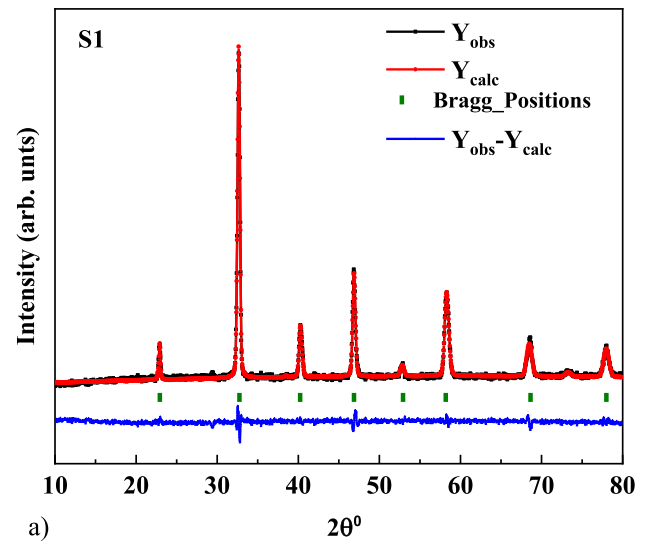
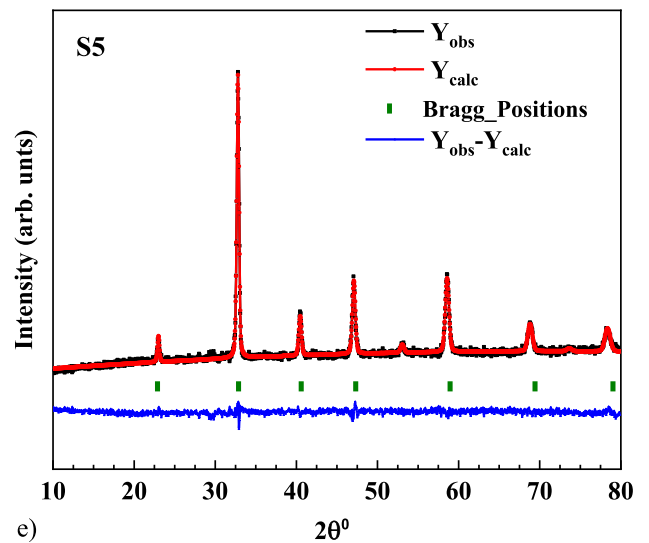
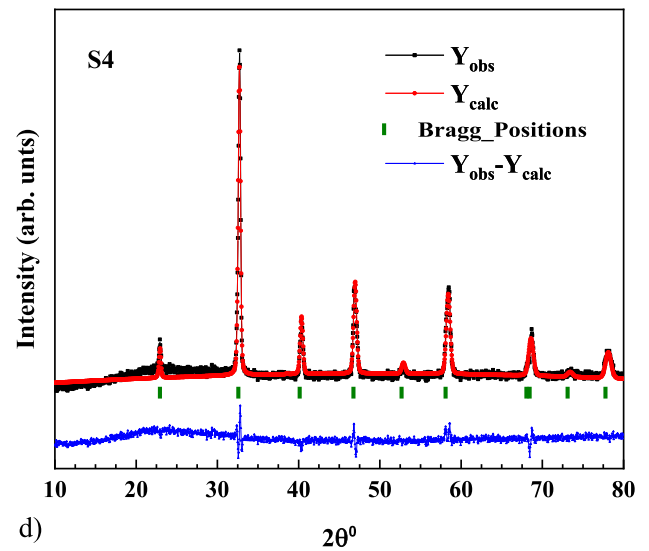


Fig. 3 continued



Substitution in perovskite manganese is equivalent to injecting cavities, and the amount of substitution in them determines the charge carriers. Substitution in manganese changes the manganese capacity from Mn^{3+} to Mn^{4+} . The presence of Mn^{4+} ions in the composition and the crystal structure provides conditions for charge carriers to be transferred in the lattice. The Mn^{4+} ions in these compounds can be controlled by substituting the manganites. On the other hand, applying an external magnetic field causes the magnetic moments to be parallelized, which can help transfer the e_g electrons from the Mn^{3+} to Mn^{4+} ions in the composition. Therefore, applying an external magnetic field has a constructive role in the transport of load carriers and reduces the specific strength of the material [30, 31].

Figure 5 shows the specific strength measurements of the samples in the 0–9 T magnetic fields. The results show that the resistivity of the samples is reduced by applying an external magnetic field. The insulation/metal transition temperature (T_{M-I}) is shifted at low temperatures by substituting Gd^{3+} . Also, the T_{M-I} has been shifted due to the applying external magnetic field to higher temperatures. Regarding the displacement of the TM-I to higher temperatures due to the external magnetic field, we can point to the larger share of the external field compared to the share of thermal energy in creating electrical order. Gd^{3+} substitution has also led to T_{M-I} displacement, which can be very important in using these compounds in magnetic refrigerators at room temperature [1, 37, 38]. Also, no effect of electrical hysteresis is observed in the diagrams, which indicates the homogeneity of the samples [39]. The T_{M-I} and Debye temperature of samples in terms of Gd^{3+} Substitution and magnetic field changes are reported in Table 3.

The results also show that resistance increases with increasing Gd substitution. Also, the T_{M-I} decreases with increasing Gd substitution. The substitution on the grain surface causes an increase in spin irregularity and, as a result, the weakness of spin-dependent tunneling. Therefore, with increasing doping, the T_{M-I} decreases (see Table 3).

Fig. 4 FESEM images and the distribution function of **a** S1, **b** S2, **c** S3, **d** S4, and **e** S5 samples

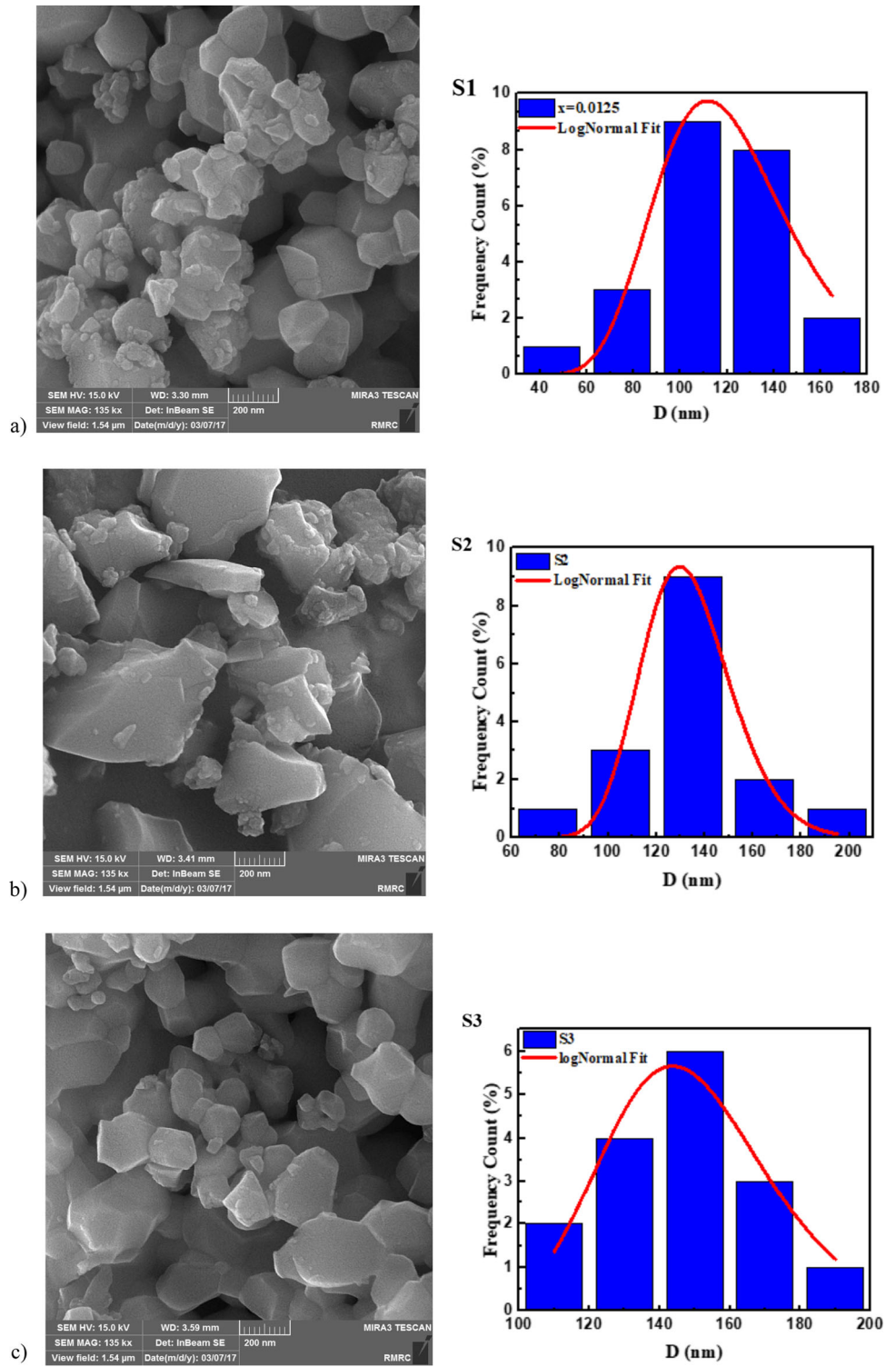


Fig. 4 continued

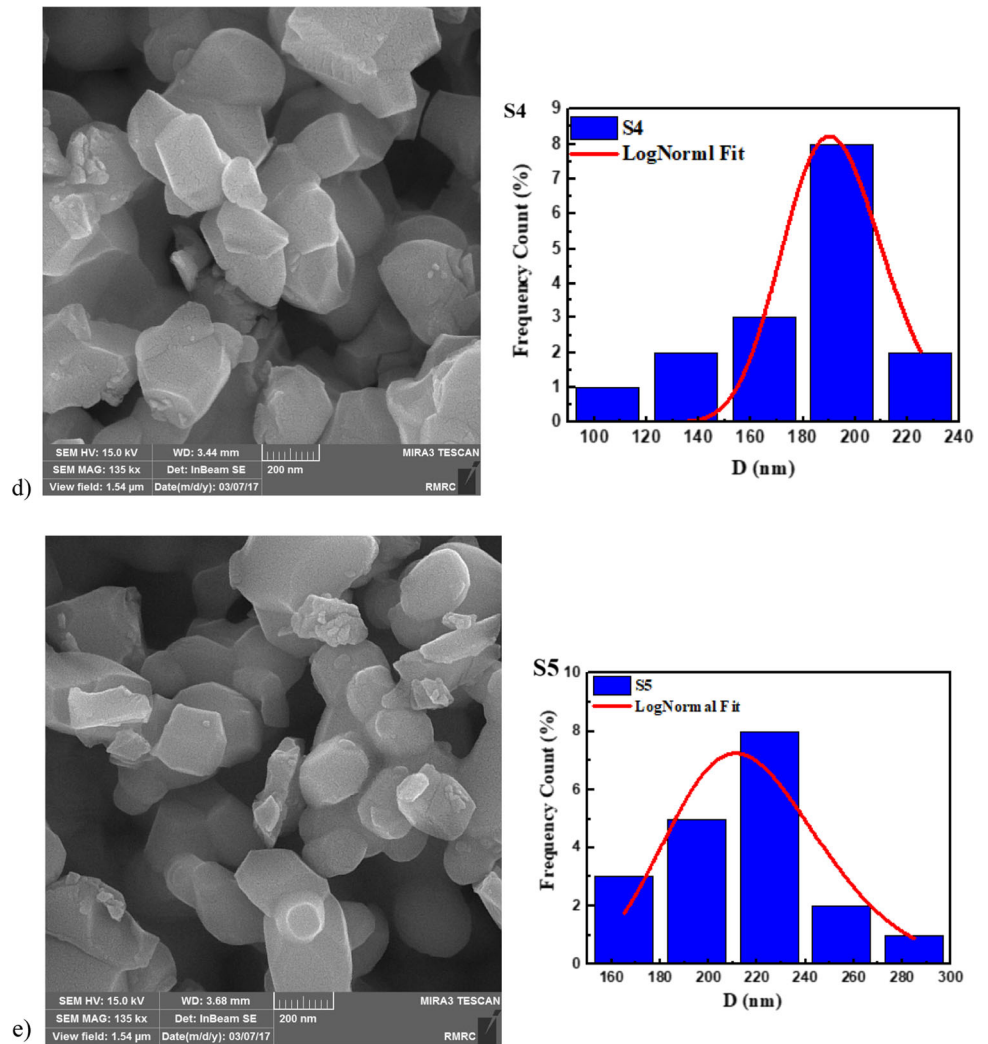


Table 2 Average particle size and standard deviation of samples

Samples	S1	S2	S3	S4	S5
$\langle D \rangle$ (nm)	122.437	133.24	149.220	193.058	218.095
σD (nm)	30.65	18.84	23.78	41.88	32.02

3.4 The bolometric application

Bolometric application of CMR LSMO manganites doped by Gd^{3+} is based on a sharp drop in temperature resistance with T_{M-I} . TCR is one of the main parameters of infrared bolometers and is defined as follows:

$$TCR = \frac{1}{\rho} \frac{d\rho}{dT} \times 100 \tag{8}$$

here ρ and T represent the resistivity of the temperature. Therefore, The TCR value is the direct result of electric resistance and M-I transition steepness, which determine our samples' application in cooled or uncooled bolometers. Figure 6 represents the TCR change of samples vs temperature in $B = 0$ T. Figure 6 shows that the TCR curve has a nonlinear increasing trend. Generally, Gd succession changes bond lengths and angles. Changes in bond lengths and angles can aggravate the dual-exchange and super-exchange interaction power and change the magnetic order. Changing the magnetic order at the nanoparticle surface increases spin scattering and reduces the likelihood of tunneling between grains. The results showed that increasing the amount of Gd substitution due to increases in the dispersion at the grain boundary and the spin irregularity increases the resistance of the sample. Previous studies have also obtained similar results. For instance, Xiaohan et al. [40] showed that the sample's resistance increases with increasing the substitution in $La_{1-x}Sr_xMnO_3$ structures.

Fig. 5 The resistance changes in terms of temperature for **a** S1, **b** S2, **c** S3, **d** S4, and **e** S5 samples at different magnetic fields

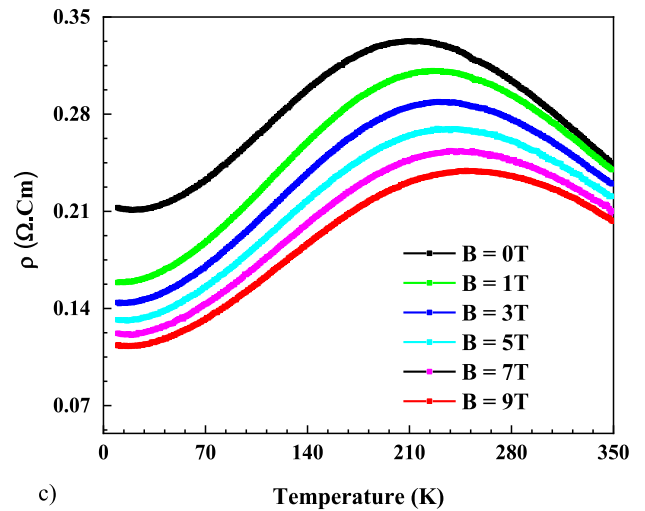
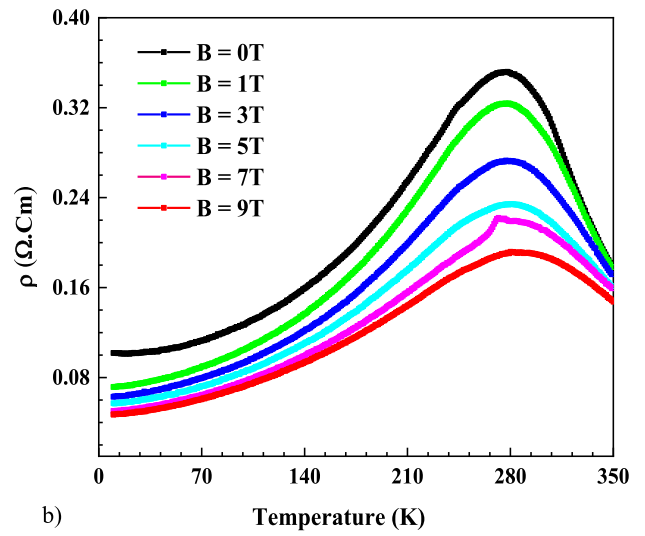
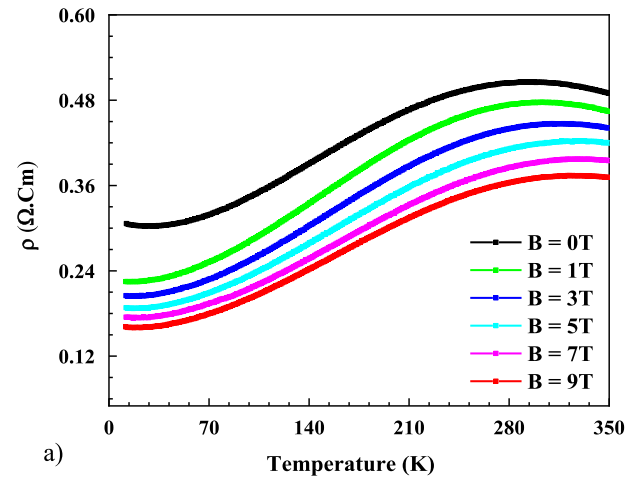


Fig. 5 continued

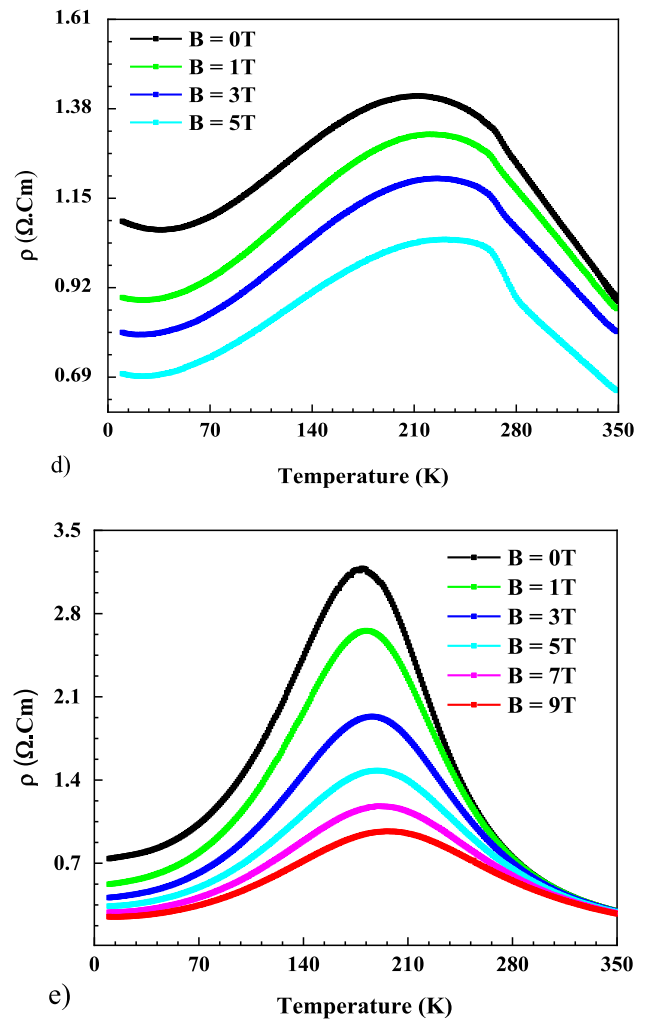


Table 3 The TM-I and Debye temperature of samples in terms of Gd³⁺ substitution and magnetic field changes

Sample	$B = 0 \text{ T}$ T_{M-I}	$B = 1 \text{ T}$ T_{M-I}	$B = 3 \text{ T}$ T_{M-I}	$B = 5 \text{ T}$ T_{M-I}	$B = 7 \text{ T}$ T_{M-I}	$B = 9 \text{ T}$ T_{M-I}
S1	297.37	303.21	317.95	320.28	330.28	324.45
S2	277.92	278.92	276.91	278.92	279.91	280.06
S3	213.93	225.94	231.94	236.93	244.94	280.06
S4	211.96	221.95	225.96	230.96		
S5	178.93	181.94	185.94	188.94	190.93	196.04

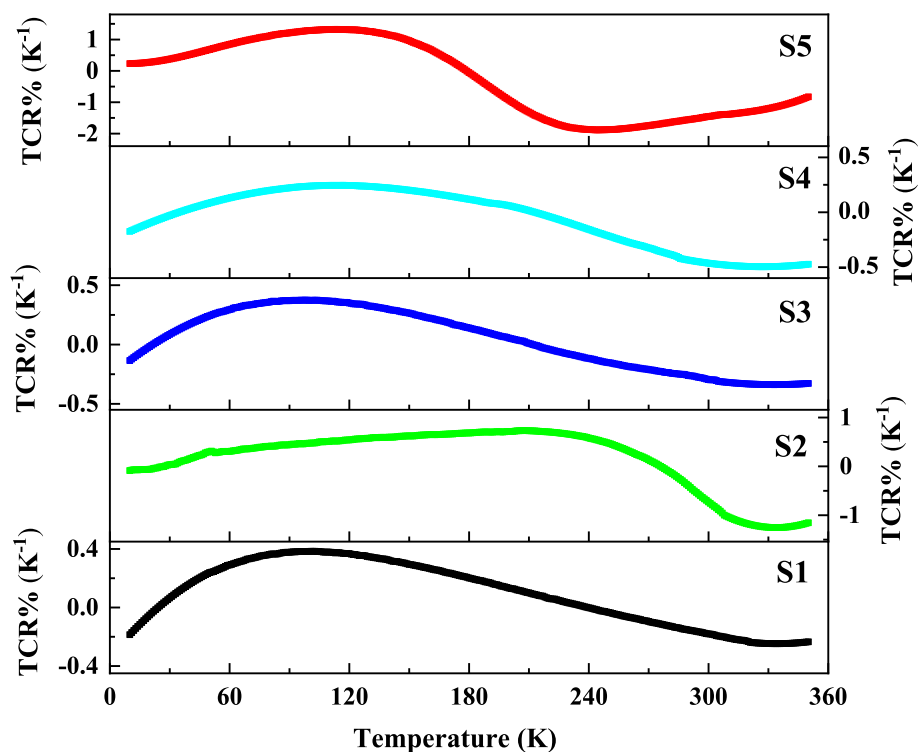
Maximum TCR% can be seen in sample $x = 0.3$ around -1.88% in 244 K, which can be a proper candidate for further investigations and cooled infrared image sensing (bolometer) modifications. Furthermore, in sample $x = 0.025$, we have a peak of 334 K (room temperature) around -1.25% , which shows potential for uncooled application in bolometric sensors.

Magnetic resistance (MR) is the relative change in electrical resistance or resistivity by the application of a magnetic field, which is defined as follows:

$$MR = \frac{\rho(H) - \rho(0)}{\rho(H)} \times 100 \tag{9}$$

here, $\rho(0)$ represents the electrical resistivity in the absence of the applied field, and $\rho(H)$ represents the electrical resistivity in the presence of the applied field. MR can be positive or negative. Negative magnetoresistance means a decrease in electrical resistance, and a positive one means an increase in electrical resistance in the presence of a magnetic field. Figure 7a shows the magnetoresistance (MR) samples in magnetic fields 1–9 Tesla. As shown in the bellow figure, the MR of specimens increases with increasing magnetic field. Spin parallel alignment at Mn–O–Mn coupling may cause the ferromagnetic interactions to increase, leading to higher magnetoresistance around T_{M-I} . Previous studies have also obtained similar results. For instance, Razi et al. [41]

Fig. 6 The changes in TCR of temperature dependence in the range of 0–400 K for all samples at magnetic fields of $B = 0$ T



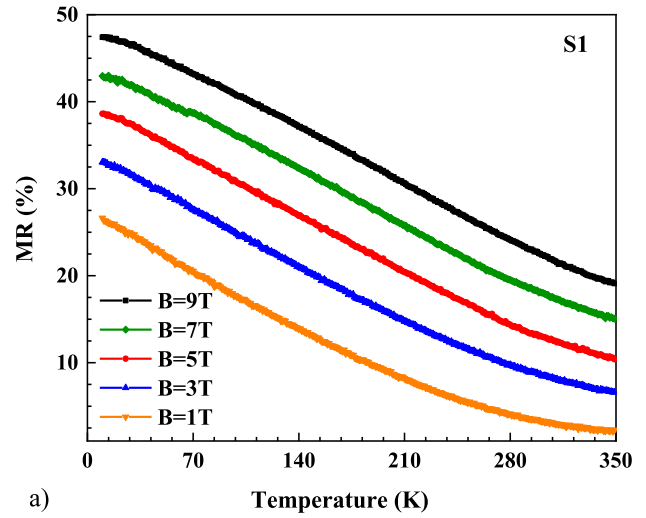
showed that MR increases with increasing magnetic field in $\text{La}_{0.7}\text{Sr}_{0.3}\text{MnO}_3$ structures. Also, Ning et al. [42] showed that MR increases with increasing magnetic field in manganites structures. In another study, Manjunatha et al. [43] showed the same results with an increasing magnetic field in other manganite structures. In addition, a high amount of MR at low temperatures may be due to grain boundary scattering of charge carriers [44, 45]. When an electron moves to the next grain, it could encounter an insulating barrier (due to either the first or second grain interface) due to reduced connectivity between the grains [46, 47]. A higher magnetic field may intensify scattering, leading to giant magnetoresistance in low temperatures.

Figure 7 revealed that the CMR effect could be seen around T_{M-I} and at low temperatures. In contrast, Spin-dependent tunneling and dispersion at the grain boundary justify increasing the magnetoresistance in the doped samples compared to the pure sample. Doping may increase the spin irregularity in the grain boundaries, increasing magnetoresistance in the doped samples [48].

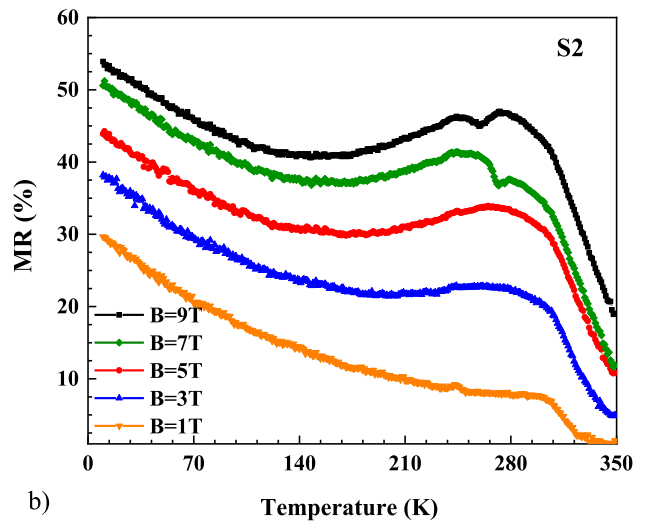
4 Conclusion

In summary, the structural and electrical characteristics of $\text{La}_{0.6-x}\text{Gd}_x\text{Sr}_{0.4}\text{MnO}_3$ ($x = 0-0.3$) are investigated. In this study, all samples were synthesized by the nitrate-complex auto-ignition technique. And the structural properties of synthesized samples are examined using the XRD and FESEM image analysis. The results showed that all samples have a rhombohedral structure with an R-3c space group. The FESEM images showed that with increasing the Gd^{3+} substitution, the average particle size of samples increased from 122.437 to 218.095 nm. The electrical properties of the samples were investigated in the temperature range of 10–350 K, and the magnetic fields are 0–9 T. The results showed that with increasing Gd^{3+} Substitution, the T_{M-I} decreases. For example, in the $x = 0$ sample, the T_{M-I} decreased from 297.37 to 324.45 K. On the other hand, increasing the magnetic field leads to an increase in the T_{M-I} . This increase is due to changes in spin irregularity at the grain boundary. The bolometric properties showed that the maximum percentage of TCR could be seen in the sample $x = 0.3$ at 244 K (around -1.88%), which can be a proper candidate for further investigations and modifications for cooled infrared image sensing (bolometer). Finally, the study of the MR properties of the samples showed that with an increasing magnetic field, the samples' resistance increased. This change is due to a decrease in spin scattering in grain boundaries.

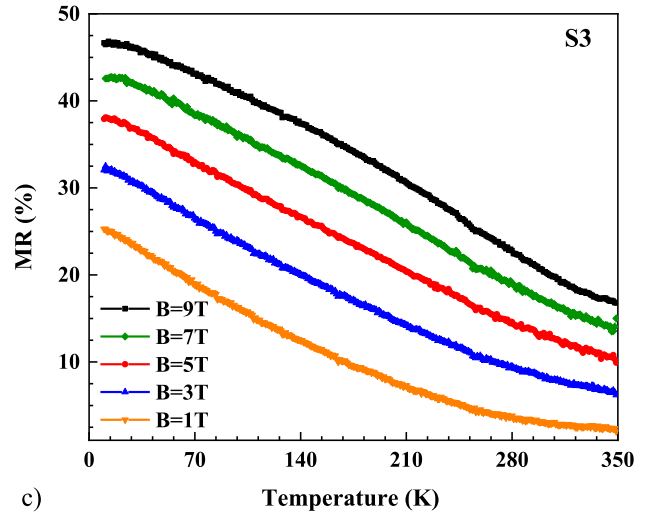
Fig. 7 The change in the magnetoresistance (MR) of **a** S1, **b** S2, **c** S3, **d** S4, and **e** S5 samples in the presence of different magnetic fields (1–9 T)



a)

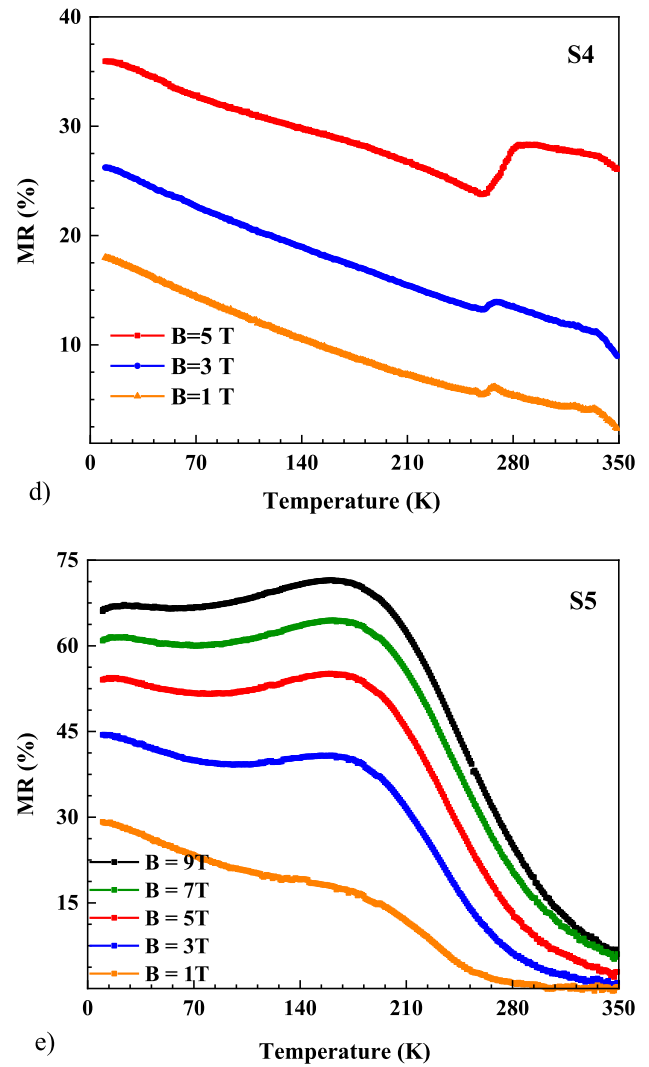


b)



c)

Fig. 7 continued



Acknowledgements The experimental facilities provided by Dr. F. Razavi are thankfully acknowledged.

Author contributions All authors contributed to the study's conception and design. Material preparation, data collection and analysis were performed by Mohammad Hossein Ehsani, Alireza Miri and Shadi Esmaeilli. Miss Esmaeilli and Mr Miri wrote the first draft of the manuscript, and Dr Ehsani commented on previous versions. All authors read and approved the final manuscript.

Funding The authors declare that no funds, grants, or other support were received during the preparation of this manuscript. The authors have no relevant financial or non-financial interests to disclose.

Data Availability Statements This manuscript has associated data in a data repository. [Authors' comment: Authors can confirm that all data are original and included in the article, and Data are available on request from the authors after publication.]

References

1. G.M. Amara, A. Dhahri, J. Dhahri, E. Hlil, Correlation between magnetic and electric properties based on the critical behavior of resistivity and percolation model of $\text{La}_{0.8}\text{Ba}_{0.1}\text{Ca}_{0.1}\text{MnO}_3$ polycrystalline. *RSC Adv.* 7(18), 10928–10938 (2017)
2. S. Jin, T.H. Tiefel, M. McCormack, R. Fastnacht, R. Ramesh, L. Chen, Thousandfold change in resistivity in magnetoresistive La–Ca–Mn–O films. *Science* 264(5157), 413–415 (1994)

3. A. Ramirez, Colossal magnetoresistance. *J. Phys. Condens. Matter* **9**(39), 8171 (1997)
4. Y. Tokura, N. Nagaosa, Orbital physics in transition-metal oxides. *Science* **288**(5465), 462–468 (2000)
5. E. Dagotto, Open questions in CMR manganites, relevance of clustered states and analogies with other compounds including the cuprates. *New J. Phys.* **7**(1), 67 (2005)
6. M. Ehsani, T. Raoufi, F. Razavi, Impact of Gd ion substitution on the magneto-caloric effect of $\text{La}_{0.6-x}\text{Gd}_x\text{Sr}_{0.4}\text{MnO}_3$ ($x = 0, 0.0125, 0.05, 0.10$) manganites. *J. Magn. Magn. Mater.* **475**, 484–492 (2019)
7. M. Ehsani, M. Ghazi, P. Kameli, J. Moradi, Size dependence of electrical properties of $\text{La}_{0.8}\text{Sr}_{0.2}\text{MnO}_3$ nanoparticles. *J. Supercond. Novel Magn.* **29**(11), 2969–2977 (2016)
8. M. Romero et al., The effect of manganite nanoparticle addition on the low field magnetoresistance of polyaniline. *J. Mater. Chem. C* **3**(46), 12040–12047 (2015)
9. S. Giri, M. Patra, S. Majumdar, Exchange bias effect in alloys and compounds. *J. Phys. Condens. Matter* **23**(7), 073201 (2011)
10. J. Nogués et al., Exchange bias in nanostructures. *Phys. Rep.* **422**(3), 65–117 (2005)
11. A. Rostamnejadi et al., Conventional and inverse magnetocaloric effects in $\text{La}_{0.45}\text{Sr}_{0.55}\text{MnO}_3$ nanoparticles. *J. Appl. Phys.* **110**(4), 043905 (2011)
12. A. Rostamnejadi, M. Venkatesan, P. Kameli, H. Salamat, J. Coey, Magnetocaloric effect in $\text{La}_{0.67}\text{Sr}_{0.33}\text{MnO}_3$ manganite above room temperature. *J. Magn. Mag. Mater.* **323**(16), 2214–2218 (2011)
13. M. Bandyopadhyay, S. Dattagupta, Memory in nanomagnetic systems: Superparamagnetism versus spin-glass behavior. *Phys. Rev. B* **74**(21), 214410 (2006)
14. R. Bhowmik, A. Poddar, R. Ranganathan, C. Mazumdar, Magnetism of crystalline and amorphous $\text{La}_{0.67}\text{Ca}_{0.33}\text{MnO}_3$ nanoparticles. *J. Appl. Phys.* **105**(11), 113909 (2009)
15. Z. Jirák et al., Ferromagnetism versus charge ordering in the $\text{Pr}_{0.5}\text{Ca}_{0.5}\text{MnO}_3$ and $\text{La}_{0.5}\text{Ca}_{0.5}\text{MnO}_3$ nanocrystals. *Phys. Rev. B* **81**(2), 024403 (2010)
16. J. Curiale et al., Magnetic dead layer in ferromagnetic manganite nanoparticles. *Appl. Phys. Lett.* **95**(4), 043106 (2009)
17. M.B. Salamon, M. Jaime, The physics of manganites: structure and transport. *Rev. Mod. Phys.* **73**(3), 583 (2001)
18. P. Siwach, H. Singh, O. Srivastava, Low field magnetotransport in manganites. *J. Phys. Condens. Matter* **20**(27), 273201 (2008)
19. X. Li, A. Gupta, G. Xiao, G. Gong, Low-field magnetoresistive properties of polycrystalline and epitaxial perovskite manganite films. *Appl. Phys. Lett.* **71**(8), 1124–1126 (1997)
20. J. Rivas, L. Hueso, A. Fondado, F. Rivadulla, M. Lopez-Quintela, Low field magnetoresistance effects in fine particles of $\text{La}_{0.67}\text{Ca}_{0.33}\text{MnO}_3$ perovskites. *J. Magn. Magn. Mater.* **221**(1–2), 57–62 (2000)
21. J. Hu, H. Qin, J. Chen, Z. Wang, Enhancement of room temperature magnetoresistance in $\text{La}_{0.67}\text{Sr}_{0.33}\text{Mn}_{1-x}\text{Ti}_x\text{O}_3$ manganites. *Mater. Sci. Eng. B* **90**(1–2), 146–148 (2002)
22. M. Laguna-Bercero, A.R. Hanifi, T.H. Etsell, P. Sarkar, V. Orera, Microtubular solid oxide fuel cells with lanthanum strontium manganite infiltrated cathodes. *Int. J. Hydr. Energy* **40**(15), 5469–5474 (2015)
23. T. Raoufi, M. Ehsani, D.S. Khoshnoud, Critical behavior near the paramagnetic to ferromagnetic phase transition temperature in $\text{La}_{0.6}\text{Sr}_{0.4}\text{MnO}_3$ ceramic: a comparison between sol-gel and solid state process. *Ceram. Int.* **43**(6), 5204–5215 (2017)
24. U. Yu, Y. Jo, B. Min, Magnetic phase diagram of doped CMR manganites. *Physica B* **328**(1–2), 117–119 (2003)
25. Z. Jirák, J. Kuličková, V. Herynek, M. Maryško, J. Koktan, O. Kaman, Titania-coated manganite nanoparticles: synthesis of the shell, characterization and MRI properties. *J. Magn. Magn. Mater.* **427**, 245–250 (2017)
26. A. Dhahri, J. Dhahri, E. Dhahri, Effect of potassium doping on physical properties of perovskites $\text{La}_{0.8}\text{Cd}_{0.2-x}\text{K}_x\text{MnO}_3$. *J. Alloys Compd.* **489**(1), 9–12 (2010)
27. A. Zahrin, N.A. Azhar, N. Ibrahim, Z. Mohamed, Structural, magnetic, and electrical properties and magnetoresistance of monovalent K-substituted $\text{La}_{0.7}\text{Ba}_{0.3-x}\text{K}_x\text{MnO}_3$ ($x = 0$ and 0.04) manganite. *Condens. Matter* **7**(3), 51 (2022)
28. M. Ehsani, T. Raoufi, Effect of Gd substitution on the critical scaling of the ferromagnetic transition of $\text{La}_{0.6-x}\text{Gd}_x\text{Sr}_{0.4}\text{MnO}_3$ ($x = 0, 0.05, 0.1$) manganite. *J. Alloys Compd.* **769**, 649–659 (2018)
29. S. Vadnala, S. Asthana, Magnetocaloric effect and critical field analysis in Eu substituted $\text{La}_{0.7-x}\text{Eu}_x\text{Sr}_{0.3}\text{MnO}_3$ ($x = 0.0, 0.1, 0.2, 0.3$) manganites. *J. Magn. Magn. Mater.* **446**, 68–79 (2018)
30. D. Li, Q. Chen, Z. Li, Y. Li, H. Zhang, Y. Zhang, Effects of silver doping on structure and electrical properties of $\text{La}_{0.67}\text{Ca}_{0.23}\text{K}_{0.1}\text{MnO}_3$ polycrystalline ceramic. *Ceram. Int.* **44**(3), 3448–3453 (2018)
31. A. Zaidi, T. Alharbi, J. Dhahri, S. Alzobaidi, M. Zaidi, E. Hlil, LaPbKMnO perovskites synthesized by sol-gel method: the effect of potassium substitution on the magnetic and electrical properties. *Appl. Phys. A Mater. Sci. Process.* **123**, 1 (2017)
32. L. Nie et al., Selective synthesis of LaF 3 and NaLaF 4 nanocrystals via lanthanide ion doping. *J. Mater. Chem. C* **5**(35), 9188–9193 (2017)
33. S. Hosseininejad, M. Ehsani, S. Esmaili, Structural and magnetic properties of yttrium-substituted $\text{La}_{0.6-x}\text{Y}_x\text{Sr}_{0.4}\text{MnO}_3$ ($x = 0–0.3$). *Ceram. Int.* **47**(8), 11536–11546 (2021)
34. S. Esmaili, M. Ehsani, M. Fazli, Structural, optical and photocatalytic properties of $\text{La}_{0.7}\text{Ba}_{0.3}\text{MnO}_3$ nanoparticles prepared by microwave method. *Chem. Phys.* **529**, 110576 (2020)
35. A. Gholizadeh, A. Malekzadeh, Structural and redox features of $\text{La}_{0.7}\text{Bi}_{0.3}\text{Mn}_{1-x}\text{Co}_x\text{O}_3$ nanoperovskites for ethane combustion and CO oxidation. *Int. J. Appl. Ceram. Technol.* **14**(3), 404–412 (2017)
36. A. Bhalla, R. Guo, R. Roy, The perovskite structure—a review of its role in ceramic science and technology. *Mater. Res. Innovat.* **4**(1), 3–26 (2000)
37. M. Ehsani, P. Kameli, F. Razavi, M. Ghazi, B. Aslibeiki, Influence of Sm-doping on the structural, magnetic, and electrical properties of $\text{La}_{0.8-x}\text{Sm}_x\text{Sr}_{0.2}\text{MnO}_3$ ($0 < x < 0.45$) manganites. *J. Alloys Compd.* **579**, 406–414 (2013)
38. M.A. Gdaiem, A. Dhahri, J. Dhahri, E. Hlil, Investigation of the magnetocaloric effect and the electrical properties of $\text{La}_{0.8}\text{Ba}_{0.1}\text{Ca}_{0.1}\text{Mn}_{0.85}\text{Co}_{0.15}\text{O}_3$ oxide manganite. *Mater. Res. Bull.* **88**, 91–97 (2017)
39. Y. Choudhary et al., effect of rare-earth substitution at La-site on structural, electrical and thermoelectric properties of $\text{La}_{0.7-x}\text{RE}_x\text{Sr}_{0.3}\text{MnO}_3$ compounds ($x = 0, 0.2, 0.3$; RE = Eu, Gd, Y). *J. Magn. Magn. Mater.* **451**, 110–120 (2018)
40. X. Yu, T. Sun, Q. Chen, Y. Duan, X. Liu, Modulation of room-temperature TCR and MR in $\text{La}_{1-x}\text{Sr}_x\text{MnO}_3$ polycrystalline ceramics via Sr doping. *J. Sol-Gel. Sci. Technol.* **90**(2), 221–229 (2019)
41. Z.J. Razi, S. Sebt, A. Khajehzadeh, Magnetoresistance temperature dependence of LSMO and LBMO perovskite manganites. *J. Theor. Appl. Phys.* **12**(4), 243–248 (2018)
42. X. Ning, Z. Wang, Z. Zhang, Large, temperature-tunable low-field magnetoresistance in $\text{La}_{0.7}\text{Sr}_{0.3}\text{MnO}_3$: NiO nanocomposite films modulated by microstructures. *Adv. Funct. Mater.* **24**(34), 5393–5401 (2014)
43. S. Manjunatha, A. Rao, G. Okram, Investigation on structural, magneto-transport, magnetic and thermal properties of $\text{La}_{0.8}\text{Ca}_{0.2-x}\text{Ba}_x\text{MnO}_3$ ($0 \leq x \leq 0.2$) manganites. *J. Alloys Compd.* **640**, 154–161 (2015)

44. H. Ju, H. Sohn, Role of grain boundaries in double exchange manganite oxides $\text{La}_{1-x}\text{A}_x\text{MnO}_3$ (A= Ba, Ca). *Solid State Commun.* **102**(6), 463–466 (1997)
45. S. Ju, H. Sun, Z.-Y. Li, Study of field dependence of magnetoresistance of polycrystalline perovskite manganites. *Phys. Lett. A* **300**(6), 666–671 (2002)
46. A. De Andres, M. Garcia-Hernández, J. Martinez, C. Prieto, Low-temperature magnetoresistance in polycrystalline manganites: connectivity versus grain size. *Appl. Phys. Lett.* **74**(25), 3884–3886 (1999)
47. A. De Andres, M. Garcia-Hernandez, J. Martinez, Conduction channels and magnetoresistance in polycrystalline manganites. *Phys. Rev. B* **60**(10), 7328 (1999)
48. M.K. Verma, N.D. Sharma, S. Sharma, N. Choudhary, D. Singh, High magnetoresistance in $\text{La}_{0.5}\text{Nd}_{0.15}\text{Ca}_{0.25}\text{A}_{0.1}\text{MnO}_3$ (A= Ca, Li, Na, K) CMR manganites: Correlation between their magnetic and electrical properties. *Mater. Res. Bull.* **125**, 110813 (2020)

Springer Nature or its licensor (e.g. a society or other partner) holds exclusive rights to this article under a publishing agreement with the author(s) or other rightsholder(s); author self-archiving of the accepted manuscript version of this article is solely governed by the terms of such publishing agreement and applicable law.